Production Engineering (2022) 16:797–809
https://doi.org/10.1007/s11740-022-01139-6

PRODUCTION PROCESS

Hybrid manufacturing: influence of material properties during micro milling of different additively manufactured AISI 316L

Sebastian Greco[1] · Marc Schmidt[1] · Katja Klauer[1] · Benjamin Kirsch[1] · Jan C. Aurich[1]

Received: 21 March 2022 / Accepted: 17 May 2022 / Published online: 7 June 2022

Abstract
Additive manufacturing (AM) enables the production of components with a high degree of individualization at constant manufacturing effort, which is why additive manufacturing is increasingly applied in industrial processes. However, additively produced surfaces do not meet the requirements for functional surfaces, which is why subsequent machining is mandatory for most of AM-workpieces. Further, the performance of many functional surfaces can be enhanced by microstructuring. The combination of both AM and subtractive processes is referred to as hybrid manufacturing. In this paper, the hybrid manufacturing of AISI 316L is investigated. The two AM technologies laser-based powder bed fusion (L-PBF) and high-speed laser directed energy deposition (HS L-DED) are used to produce workpieces which are subsequently machined by micro milling (tool diameter d = 100 µm). The machining results were evaluated based on tool wear, burr formation, process forces and the generated topography. Those indicated differences in the machinability of materials produced by L-PBF and HS L-DED which were attributed to different microstructural properties.

Keywords Hybrid manufacturing · Additive manufacturing · Micro milling · Laser-based powder bed fusion · High-speed laser directed energy deposition

1 Introduction

Additive manufacturing (AM) processes are described by the layer-by-layer build-up of a geometry by adding volume elements [1]. AM processes are characterized by their entirely digital process chain and, due to tool-free production [2], by increased flexibility and the possibility of producing small quantities economically. Furthermore, increased component complexity has almost no influence on the manufacturing effort when using AM, which is why an increased degree of individualization and functional integration can be implemented [3].

One obstacle to the large-scale use of AM of metallic materials is the generally inadequate surface quality [4]. The surface roughness is defined by the parameters of the powdered raw material used for AM and the characteristics of the melt paths during the process [5]. In order to produce suitable functional surfaces, the additively produced near-net-shape components are usually finished by machining [6]. This sequential use of additive and subtractive manufacturing processes is referred to as hybrid manufacturing [7]. One promising example of hybrid manufacturing is the production of implants, which are usually specially adapted geometries [8]. Further, microstructured surfaces on implants might enhance medical applications e.g., via an improved healing time.

With regard to hybrid manufacturing, separate studies have been carried out, many of them on either additive or subtractive parts of the process chain. The material properties of additively produced metals are determined by the process parameters used during AM [9]. Choo et al. showed that the relative density of AISI 316L produced by laser-based powder bed fusion (L-PBF) is directly related to the laser power used during AM [10]. Reduced laser power led to increased porosity. Additively manufactured materials exhibit a variety of inhomogenous properties such as pores [11], changing residual stresses [12] or different grain sizes and orientations depending on the AM parameters [13]. In addition, the material properties of material of the same specification differ depending on whether they were produced additively or by casting [14].

✉ Marc Schmidt
Marc.schmidt@mv.uni-kl.de

[1] Institute for Manufacturing Technology and Production Systems, Technische Universität Kaiserslautern, Gottlieb-Daimler-Str., 67663 Kaiserslautern, Germany

These differences are also evident when comparing their machinability. Campos et al. investigated micro milling of additively produced (L-PBF) and casted Ti6Al4V [15]. Despite an increased strength and hardness of the L-PBF material, lower process forces and reduced burr formation were observed during machining. This was attributed to a lower tool wear during machining of L-PBF workpieces. Differences in machining can also be observed in materials produced by laser directed energy deposition (L-DED). Kallel et al. conducted studies on face milling of Ti6Al4V produced by L-DED and casting, which revealed an increased minimum chip thickness when machining L-DED workpieces [16].

Due to size effects [17], process parameters like the minimum chip thickness have a special significance in small-scaled machining processes such as micro milling [18]. The significantly changed ratio between cutting edge radius and chip thickness during micro milling can lead to elastic and plastic deformation of material instead of its separation, which is reffered to as ploughing [19] and reduces the accuracy of micro machined surfaces [20]. In addition to this example of a scale effect, inhomogenous material properties are also decisive for the machining result of micro milling processes. In previous studies carried out at our institute, Kieren-Ehses et al. showed that different grain orientations within the material removal have an influence on the machined surface and process forces during micro milling of titanium [21].

Both additive manufacturing processes, L-PBF and DED, are widely used in industrial applications and are proven to lead to different machining results. The machining of materials produced by high-speed laser directed energy deposition (HS L-DED, which is an evolution of DED) is hardly researched at all. In this paper, the hybrid manufacturing of AISI 316L is investigated using L-PBF, HS L-DED and micro milling (tool diameter d = 100 µm). The influence of the different material properties, resulting from varied AM processes, on the process result of micro milling is analyzed and compared. For this purpose, the materials' relative density, microhardness and microstructure are characterized by the Archimedes method, hardness measurements, etched micrographs and EBSD-scans. The machinability is evaluated based on process forces, topography, burr formation and tool wear. The experimental investigations are also executed on casted material of the same specification, which will be referred to as reference material in this paper.

2 Additive manufacturing

2.1 Laser-based powder bed fusion

The machine system Mlab Cusing by Conceptlaser* was used for the L-PBF of the workpieces. This AM system is equipped with a fiber laser (Nd:YAG, λ = 1064 nm, laser beam diameter ~ 50 µm) with a maximum power of 100 W. The workpiece geometry was defined as a cube with an edge length of 8 mm. The workpieces were fixed to the building platform by columnar support structures and a chessboard sanning strategy with 5 × 5 mm block size, was used [22]. The powder used to produce the workpieces had a particle size distribution of 10–45 µm (manufacturer's information). The workpieces were aligned along the L-PBF system's coordinate system so that the orientation of the layers and the build-up direction could be determined even after the workpieces had been separated from the building platform. During L-PBF the building platform was not heated. Nitrogen was used to create an inert atmosphere. The L-PBF process parameters are shown in Table 1 and are based on previous studies of relative density optimization [5].

2.2 High-speed laser directed energy deposition

HS L-DED is an adaption of laser directed energy deposition (L-DED) to achieve higher build-up rates. Li et al. explained that during HS L-DED, the focus of the metal powder and the laser coincide above the workpiece's surface, which causes the powder to already melt in the air [23]. In this way, the time required for the powder to melt in the melt pool at a component's surface, which is characterisitic for L-DED, is eliminated. Transmitted laser radition of HS L-DED also induces a melt pool beneath the focus of powder and laser. However, due to the smaller amount of incoming radition, this melt pool and the respective heat affected zone (HAZ) are much smaller than those created during L-DED [24]. A schematic representation of HS L-DED and the position of the focal plane is shown in Fig. 1.

A TLC 1005 laser welding cell and a TruDisk5001 laser beam source with 5 kW maximum laser power (λ = 1030 nm) from Trumpf* equipped with an ILT-Aachen-EHLA-Coax D40 powder nozzle were used to produce the HS L-DED workpieces. The workpieces were built directly onto the building platform, which is common for L-DED processes. The powder used in this study has a particle size distribution of 15–45 µm (manufacturer's information). During HS L-DED argon was used to generate a local inert

Table 1 Parameters of L-PBF

Parameter	Value
Laser power	50 W
Layer thickness	25 µm
Hatch distance	84 µm
Scanning speed	200 mm/s
Scanning strategy	5 × 5 mm chessboard

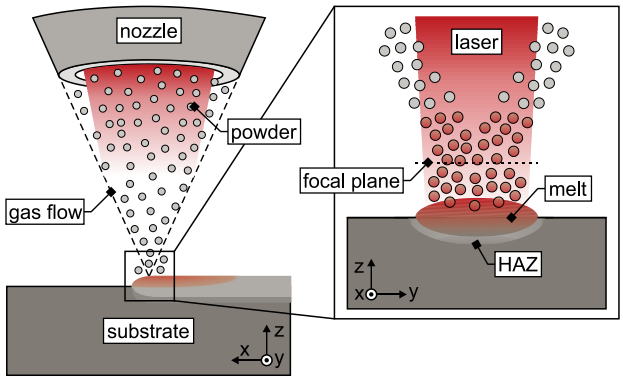

Fig. 1 Schematic representation of high-speed laser directed energy deposition (HS L-DED)

atmosphere near the melt pool. The process parameters of HS L-DED are given in Table 2.

3 Material properties

3.1 Relative density and microhardness

A decisive evaluation criterion for additively manufactured components is the relative density. This indicates the ratio of the ideal density of a defect- and pore-free volume compared to the actual measured density. The relative density was determined using the Archimedes method. For this purpose, an EMB-200-3V balance from KERN* was used to measure the sample mass in air and in water. To calculate the density, an ideal density of the material AISI 316L of $\rho_{316L} = 7.99$ g/cm^3 [26] was assumed.

Based on the Archimedes method a relative density of $99.4 \pm 0.4\%$ for the HS L-DED samples, which corresponds to an absolute density of 7.94 ± 0.03 g/cm^3, was determined. For the L-PBF samples, values of $99.1 \pm 0.1\%$ and 7.92 ± 0.01 g/cm^3 respectively were obtained.

Table 2 Parameters of HS L-DED [25]

Parameter	Value
Laser power	3300 W
Laser spot size	1.4 mm
Layer thickness	117 µm
Hatch distance	700 µm
Feed velocity	40 m/min
Powder mass flow	28.3 g/min
Scanning strategy	Bidirectional
Carrier gas flow rate (argon)	6 l/min
Shielding gas flow rate (argon)	10 l/min

For the qualitative assessment of the density and further investigations, cross sections of the samples were prepared. For this purpose, the bulk material was sectioned and prepared accordingly. A Presi* Mecatome T210 precision cutting machine was used to separate the samples. In order to minimize the thermomechanical stress on the samples during the cutting process, the pieces were cut at a feed rate of 0.02 mm/s with cooling. The separated samples were embedded, ground and polished. A Presi* Mecapress 3 embedding machine was used for embedding, and a Presi* Mecatech 334 was used for grinding and polishing. Grinding was performed with SiC abrasive paper up to a grit size of P2500, and further polishing was performed using diamond suspensions with grain sizes from 6 down to 0.05 µm. The generated cross sections of the HS L-DED and L-PBF samples can be seen in Fig. 2 and show an almost defect- and pore-free cross-sectional area for both samples. Only a few small pores can be seen, tending to be more in the L-PBF sample than in the sample produced by HS L-DED.

Microhardness measurements were carried out on the cross sections. According to DIN EN ISO 6507–1 [27], the microhardness HV0.01 (test force F = 0.098 N) was analyzed using a Buehler* MicroMet 5100 hardness tester. To determine the hardness in the bulk material, 15 hardness indentations were made and measured in the center of each specimen. The hardness measurements revealed values of 214 ± 9 HV0.01 for the HS L-DED specimen, 212 ± 14 HV0.01 for the L-PBF specimen and 193 ± 12 HV0.01 for the reference specimen.

3.2 Microstructure

For the characterization of the microstructure of the different samples, previously prepared cross sections were etched by immersion for 15–20 s in a solution of HCl, HNO_3 and acetic acid in a 15:10:1 ratio to visualize the grain structure and melt paths. Light optical micrographs of the etched specimens are shown in the upper half of Fig. 3. The melt borders of the additively manufactured specimens have been clearly visualized by etching. In the case of the HS L-DED sample,

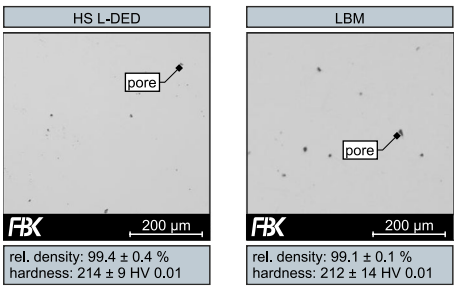

Fig. 2 Micrograph of AISI 316L produced by HS L-DED (left) and L-PBF (right)

etching made some grains visible that are elongated along the build-up direction.

As shown in studies by Ma et al. [28] and Vilaro et al. [29], the grains in additively manufactured workpieces often grow beyond the melt paths. Since the microstructure strongly influences the behavior during micromilling in any case, as demonstrated by Attansio et al. [30] and Popov et al. [31], the melt path geometry of the AM workpieces was investigated consequently. The etched cross sections were used to determine the aspect ratios of melt path width (w) to melt path height (h) for the additively manufactured specimens. These were measured on 20 randomly distributed melt paths and resulted in ratios of $w/h = 3.9 \pm 0.4$ µm for the HS L-DED specimen and $w/h = 2.1 \pm 0.3$ µm for the L-PBF specimen. The aspect ratios differ due to the different processes and the different ratios of the respective process parameters like laser power and scanning speed.

The microstructure of the reference material shows a coarse-grained structure with globular grains and clearly visible annealing twins within the grain boundaries, which is characteristic for continuously casted 316L stainless steel. Furthermore, in addition to the light optical micrographs, electron backscatter diffraction (EBSD) scans in form of inverse pole figures (IPF) are given in the lower half of Fig. 3. These are used alongside the light optical micrographs to visualize the grains and their orientation. Different grain structures are clearly visible. In particular, the EBSD studies confirm the grain elongation along the build-up direction, already observed in the light optical micrographs of the HS L-DED sample. The grains are also significantly larger than those of the L-PBF and reference samples, which can be explained by the significantly higher energy input of the process. The IPF image of the L-PBF sample also shows a slight tendency to grain elongation in the build-up direction, but the sample has significantly smaller grains compared to the HS L-DED sample. The IPF image of the reference clearly shows the globular grain structure with some annealing twins in the grains. In this context, no orientation preference in the grain structure for the different additively manufactured samples can be observed in the EBSD investigations.

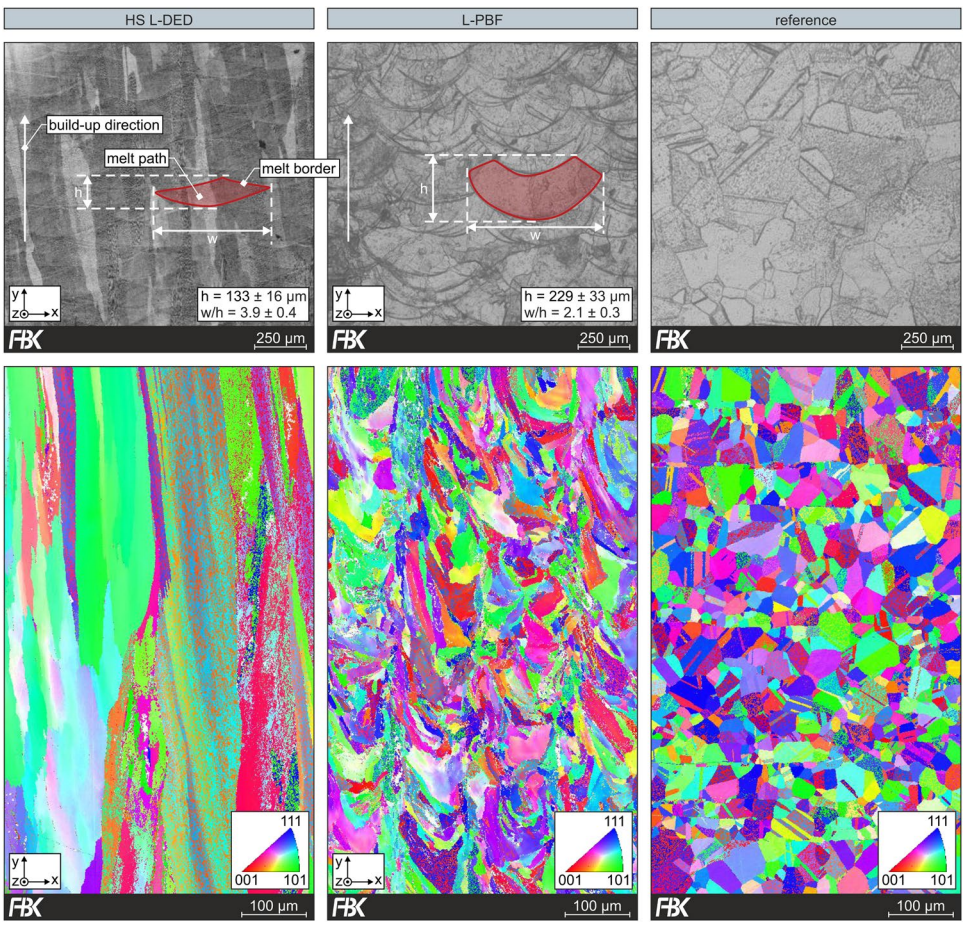

Fig. 3 EBSD-scans and etched micrographs of AISI 316L produced by HS L-DED, L-PBF and casting (reference) with y-direction equals build-up direction during AM

4 Experimental setup

The experiments were carried out using the MMC 600 H machine tool by LT Ultra*. The workpieces were glued to a workpiece holder, which in turn was directly connected to a multicomponent dynamometer by Kistler* (9119AA2) with a natural frequency ≥ 4.3 kHz for all directions. The workpieces were aligned along the machine tool's coordinate system with the aid of a tactile sensor and subsequently face milled. For this purpose, a larger milling tool (MSXH440R by NS tools*) was used. Following this, the workpieces were micro milled using single-edged cBN micro end mills with a tool diameter of d = 100 µm, 2 µm diameter tolerance and a helix angle of 20°, as specified by the manufacturer (SMEZ120 D0,100 by NS tools*). In addition, the cutting edges of the tools were analyzed using a NaniteAFM atomic force microscope by Nanosurf*. The measurements were performed using the method developed by Kieren-Ehses et al. [32]. A cutting edge radius in the range 1.5–2 µm was obtained. The machining setup as well as an enlarged view of the micro end mill can be seen in Fig. 4.

The feed travel was 72 mm, divided into 9 slots of 8 mm length each. The slots were aligned parallel to the build-up direction of L-PBF and HS L-DED (y-direction in Fig. 3). The cutting parameters are listed in Table 3 and are based on previous research on micro milling of AM materials [33].

The tests were repeated three times to better identify trends of process results. A new tool was used for each of the nine tests (three materials, three repetitions).

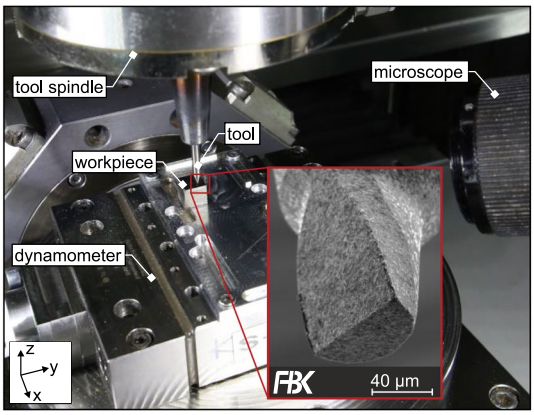

Fig. 4 Experimental setup

Table 3 Parameters of milling process

Parameter	Value
Spindle speed	25,000 rpm
Feed per tooth	1 µm/rev
Cutting depth	5 µm
Feed travel	72 mm (9 slots)

5 Measurement and evaluation

5.1 Topography and Burr formation

A confocal microscope Nanofocus µSurf Explorer* was used for topography measurement. The objective used has a 50 × magnification and a numerical aperture (NA) of 0.5. The measurement field size of this objective is 320 µm × 320 µm. Two different measurement procedures were used: Burr measurement and topography measurement in the milled slots.

5.1.1 Topography measurement in the milled slots

Measurements were taken for the evaluation of areal surface texture parameters. The measurements were taken for all tests in the 1st, 3rd, 5th, 7th and 9th slot. For the evaluation of the areal surface texture parameter, an evaluation area of 150 µm × 50 µm was extracted in the middle of a stitched topography measurement (see Fig. 5). The evaluation area was placed in the center of the measurement field. After alignment (plane fit) of the topography, the values of Sa were evaluated according to ISO 25178-2 [34] without further filtering.

5.1.2 Burr measurement

For the evaluation of burr formation, two images were taken at every first (0–8 mm) and ninth (64–72 mm) slot, both immediately at the beginning and end of the slot. In each case, a single image was taken with the measuring field size of the objective. This results in four images for each test. The images in the first slots show the burr formation before the onset of tool wear. The images in the last slots show the burr formation after the complete tested feed travel. The entire measurement length from each individual measurement was used for the burr evaluation (see Fig. 5, x- and y-direction). In the z-direction, the maximum travel distance (250 µm) of the confocal microscope's piezo was used in order to be able to quantitatively measure the entire burr height.

The quantitative burr analysis is done by the method of Medossi et al., which is a binary burr classification based on the processing of 3D surface information [35]. The main purpose of this method is to automatically identify areas of burr formation and to enable a quantitive burr

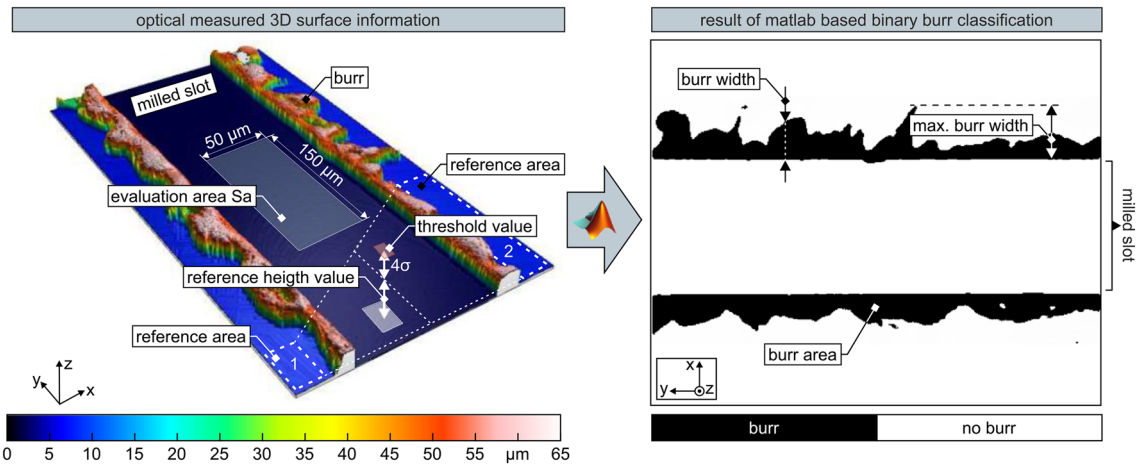

Fig. 5 Optical measured surface information and matlab based binary burr classification

analysis. The initial data and the result of this classification are shown in Fig. 5.

The procedure of the method is as follows: first, the areal surface topography of the roughness measurements is imported into Matlab*. A reference area is then specified on both sides of the milled slot, which corresponds to the face milled surface of the workpiece. An average value of the reference area's height is calculated, including all measured points inside the respective area. In order to obtain the largest possible range for stochastic evaluation of the average value, reference areas were defined on both sides of the slot. Subsequently, a fictious reference height value in the middle of the slot is determined by the arithmetic mean of the values of the two reference areas. This value will help to define a threshold above which areas with higher surfaces are identified as burr. The calculation according to Medossi et al. [35] was adapted, in order to cleary distinguish between burr and other surface defects. The threshold value is then calculated as the reference height value plus four times the averaged standard deviation of the reference height areas on both sides of the milled slot. In the next step, all pixels of the optical measured 3D surface information are checked, whether their surface height lies above or below the threshold value. The height information of all pixels above the threshold is set to 1000 µm in order to clearly distinguish from the height of the milled slot (ideal height: 0 µm) and the face milled surface (ideal height: 5 µm). After modifiying the height information, a binary image is created based on the adjusted scale of the 3D surface information. Due to the binarization, burr (numerical value = 0) can be cleary distinguished from other surfaces (numerical value = 1). The burr area is calculated by counting the pixels assigned to be burr and by the known lateral discretization of the image.

5.2 Process forces

The process forces acting on the tool during micro milling were measured by using the dynamometer 9119AA2 by Kistler*, which features a response threshold of < 0.002 N. The measured data was then processed and evaluated in Matlab*. The procedure of data processing was as follows: first, the force signals were filtered by a bandpass filter with cutoff frequencies of ± 50 Hz to the spindle's rotational frequency $f_S = 416.67$ Hz ($f_L = 366.67$ Hz and $f_H = 466.67$ Hz) to eliminate interfering signals and drifts. Subsequently, the offset of the process force was determined when the tool was not engaged. This offset was subtracted from the force signal during tool engagement, so that the resultant force was calculated. This calculated force corresponds to the length of the force vector resulting from the vector addition of the force components in x-, y-, and z-direction. Due to deviations from the set cutting depth, the process forces were normalized to the real, measured depth of the slots (N/µm). This provides a better comparability of the tests. The specific resultant force was determined by averaging over the feed travel of a slot and relating the resultant force to its respective slot depth, which might vary due to progressing tool wear.

5.3 Tool wear

The tool wear was analyzed qualitatively by comparing scanning electron microscopy (SEM) images of the tools before and after the experimental tests. Prior to the scans, all tools were cleaned for five minutes in an ultrasonic bath with isopropanol.

6 Results and discussion

During the machining experiments, tool breakage occurred after $l_f = 40$ mm during repetition 3 of the reference material. Accordingly, following figures and diagrams only show a limited amount of data for this test point wherein this early tool failure itself might be considered as a result caused by high load.

6.1 Tool wear

In Fig. 6, SEM-images of the used micro end mills are shown after completion of the feed travel of $l_f = 72$ mm or after tool breakage (reference material, repetition 3).

Different types and conditions of tool wear can be observed when comparing the used tools to the exemplarily shown new tool in Fig. 4. Micro end mills used for machining of HS L-DED and L-PBF materials show mainly adhesive wear, whereas tools used for micro milling of the reference material show mainly abrasive wear. The fact that the tools for machining the different AM materials do not show abrasive wear is due to the different microstructure and mechanical properties, resulting in a different wear behavior. The different machining behavior between additively and conventionally manufactured samples of the same material was observed before [33]. The cutting edges of the tools used for the machining of reference material cleary show wear which results in a cutting edge rounding. This favours ploughing and increasing process temperatures during machining. In addition, during repetition 3 of machining the reference material, tool breakage occurred before reaching the feed travel of $l_f = 72$ mm. A possible reason could be the formation of build-up edges, resulting in an exceeding of cutting forces that ultimately led to mechanical failure. This assumption is strengthened by the measured varying slot depths (6.3–6.5 µm). Those are significantly higher than the ideal, set slot depth of 5 µm, what can be caused by build-up edges that altered the length of the tool. Build-up edges may have also been present during other repetitions, but since they tend to rip off during machining or tool cleaning, they are not necessarily visible on SEM-images.

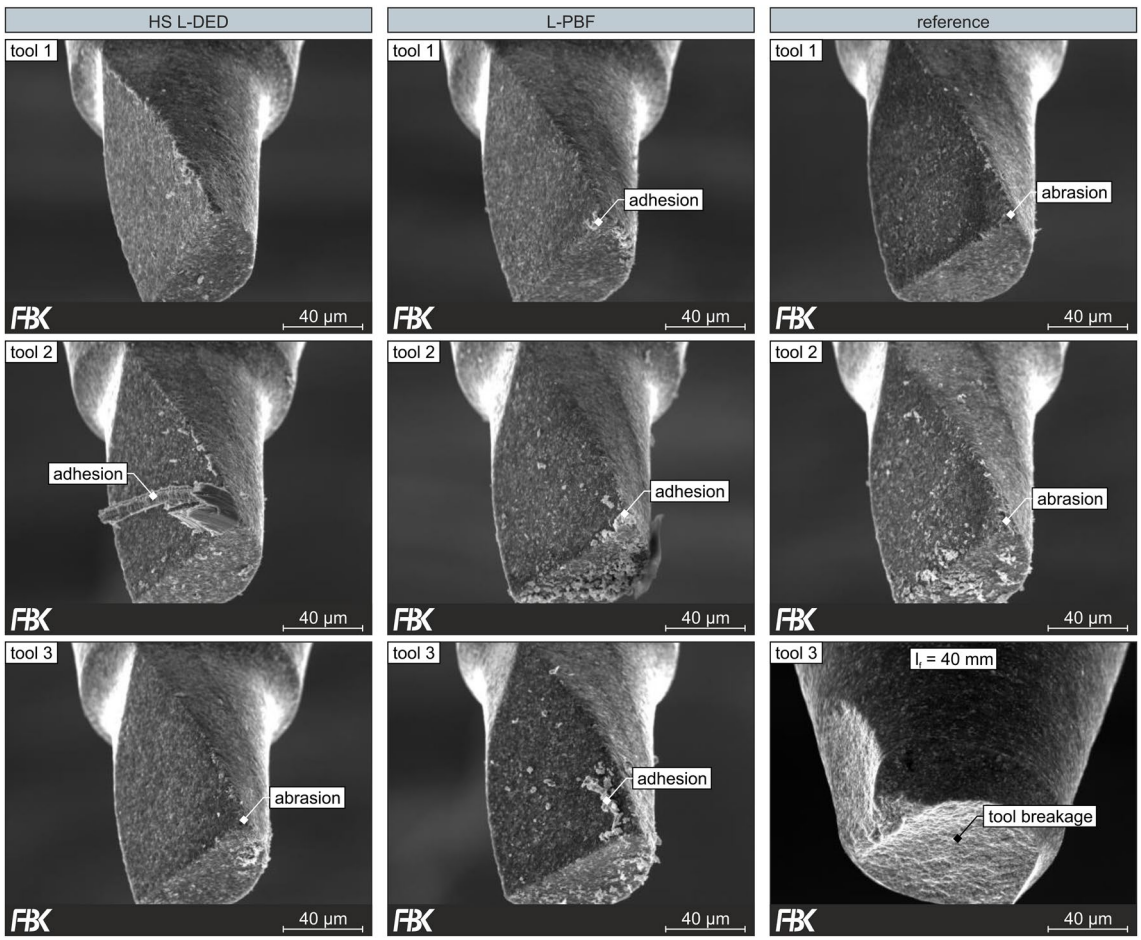

Fig. 6 SEM-images of the tools used for micro milling ($l_f = 72$ mm)

The adhesions during machining AM materials occur primarily on the tools' rake face. Adhesion is most clearly seen in repetition 2 during machining HS L-DED workpieces. Except for this large adhesion, the adhesions tend to develop in a smaller scale (e.g. L-PBF, repetition 3). In contrast to tools used for the machining of the reference material, changes in the cutting edge of the micro end mills for machining HS L-DED and L-PBF material are observed to a smaller extent.

6.2 Process forces

In Fig. 7, the specific resultant forces during micro milling of HS L-DED, L-PBF and of the reference material are shown over the feed travel. The forces of all materials tend to attain similar force values at the beginning of the feed travel ($l_f = 4$ mm), which is due to hardly any tool wear and thus similar cutting conditions. This convergence of force values at $l_f = 4$ mm is no longer present with increasing feed travel. Overall, the lowest force progression over the feed travel is found for the materials manfucatured by means of L-PBF (0.008–0.026 N/µm), highest forces were reached by the reference material (0.012–0.059 N/µm). HS L-DED materials tended to exhibit resultant forces of 0.011–0.042 N/µm. As can be seen in Fig. 7, the forces tend to increase with increasing feed treavel for the reference material due to increasing wear. The variations in the process forces when cutting the reference material are related to the formation of built-up edges and their separation.

The different levels of specific resultant forces during micro milling of HS L-DED and L-PBF materials is due to the microstructure resuting from AM and superimposed effects at grain boundaries and melt borders. The use of different AM processes results in fundamentally different grain structures, which is expressed in strong variations of the unprocessed force signals between HS L-DED and L-PBF (see excerpts in Fig. 7). The force signal of HS L-DED shows significantly more abrupt and temporary increases in the force component (z-direction). This might be caused by the different grain structures of the AM materials (compare Fig. 3). L-PBF materials exhibited a smaller grain size compared to HS L-DED workpieces. Due to the relation of the grain size and the tool diameter, it can be assumed that the micro milling tool is permanently in engagement with several grains during the machining of L-PBF materials. Micro milling through grain boundaries is thus constantly present. At grain boundaries, dislocations accumulate, and dislocation movement is hindered [36]. This leads to a material streghtening comparable to the Hall–Petch relation [37] when micro milling through grain boundaries and thus to increased cutting forces which can be detected in the force signal as a more widely spread force band. Due to the coarser grain structure of HS L-DED workpieces, the crossing of grain boundaries is significantly less frequent and can be seen in the force signal as individually occurring increases. This effect of material strengthening at grain boundaries is superimposed by identical effects when crossing melt borders. Since the direction of feed motion is parallel to the build-up direction for both AM materials, the melt paths are crossed along their height h during micro milling. The average melt path height of HS L-DED workpieces is significantly lower than that of L-PBF workpieces (see Fig. 3), which is why considerably more melt borders are crossed when machining HS L-DED workpieces. Similar to grain boundaries, dislocation movement is hindered at melt borders and leads to increased cutting forces when crossing them. L-PBF workpieces exhibit comparatively high values of melt path heights, meaning that fewer melt borders are

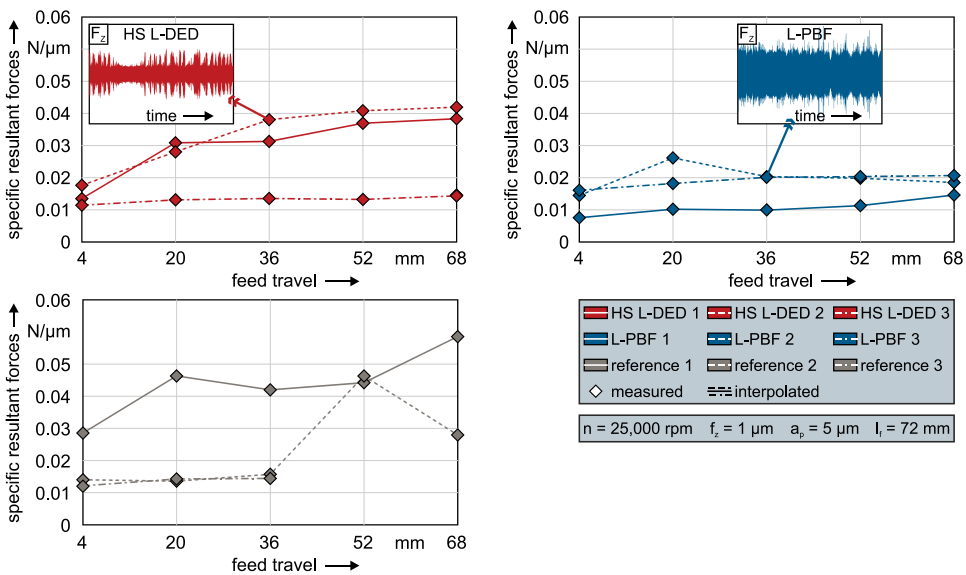

Fig. 7 Specific resultant forces over the feed travel for all examined materials

crossed during micro milling and thus a lower proportion of strengthened material needs to be machined. This lower percentage of machining of strengthened material leads to the reduced specific resultant forces during micro milling of L-PBF workpieces. The relationship between specific resultant force and microstructure of AM materials is consistent with findings from previous studies focusing on the machinability of L-PBF materials in macro- [38] and micro-scaled [33] processes. Due to a tendency of higher specific resultant forces during micro milling of HS L-DED, it was assumed that the material strengthening when crossing melt borders exceeds the material strengthening when crossing grain boundaries. Only the third test run of the HS L-DED material shows significantly lower specific forces. The three test repetitions were performed starting from the edge towards the center of the specimen. It is therefore assumed that a different material behavior is present due to a different thermal history in the center of the specimen.

The comparatively high cutting forces during micro milling of the reference material are due to superimposed effects of material properties and tool wear, both favoring ploughing. On the one hand, reference materials are much more ductile than materials of the same specification produced by AM, as shown in studies by Facchini et al. [39] and Kempen et al. [40]. Hence, this ductility promotes ploughing. On the other hand, ploughing is enhanced due to cutting edge rounding of the micro end mills, which was identified in our trials. In addition, ploughing results in increased process temperatures, which in turn lead to further softening of the material as the Young's modulus is reduced [41]. The thus overall increased ploughing during machining of reference material leads to the higher levels of specific resultant forces.

6.3 Topography

In Fig. 8, the values of the arithmetical mean height Sa over the feed travel are shown. The reference material exhibits by far the highest surface roughness. The values of Sa are significantly lower for the AM materials overall, with the values for the HS L-DED material tending to be slightly higher than for the L-PBF material.

The higher roughnesses of the reference material's machined surfaces result from material smearing. Smearing is caused when the material is not separated as chips, but plastically deformed by the cutting edge, confirmed by SEM-images in Fig. 9. The feed direction and the direction of rotation are both related to the tool. It is clearly visible that the mentioned material smearing has a higher order of magnitude than the kinematic roughness in the slots ground. The kinematic grooves, which are caused by the feed per tooth and are characteristic for milling processes, cannot be resolved with the SEM settings used, whereas the material smearing is clearly visible.

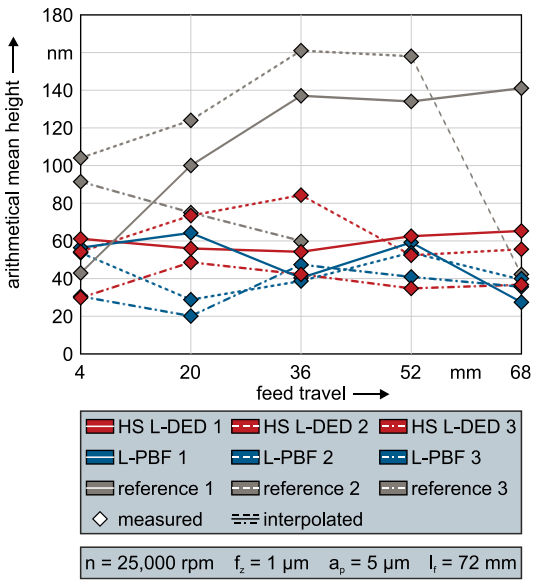

Fig. 8 Arithmetical mean height over the feed travel for all examined materials

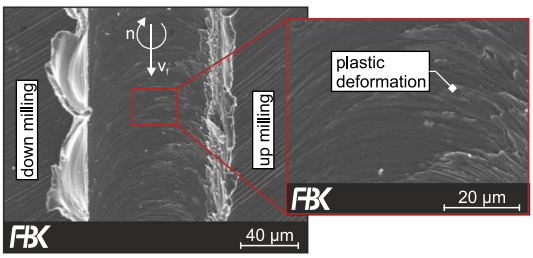

Fig. 9 Exemplary SEM-image of plastic deformation on slot bottom of reference material

When machining the reference material, plastic deformations were detected on the bottom of the milled slot dominantely on the up milling side. This is due to the chip thickness of zero when the micro end mill enters the material during up milling. The minimum chip thickness is not reached, leading to ploughing and visible plastic deformation on the slot's bottom. In down milling, the tool exits the material with a chip thickness of zero. At this side, no material smearing can be seen in the slot because the material is not pulled in. Instead, however, a large burr is formed on the down milling side.

As mentioned earlier, reference materials are significantly more ductile than AM materials of the same specification. Therefore, ploughing is reduced when micro milling AM materials and the resulting plastic deformation is much lower. The more brittle AM materials thus exhibit the characteristic kinematic roughness at the slot bottoms, which is shown in Fig. 10.

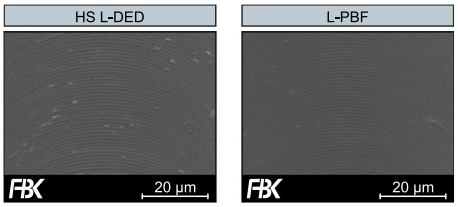

Fig. 10 Exemplary SEM-images of the slot bottom of HS L-DED and L-PBF material

6.4 Burr formation

In Fig. 11, the results of the binary burr classification immediately at the beginning of the feed travel (beginning of slot 1 $\triangleq l_f < 1$ mm) and at the end of the feed travel (end of slot 9 $\triangleq l_f > 71$ mm) are shown to illustrate the progression of burr formation over a maximum distance of feed travel. In addition, SEM-images of the milled structures at the end of the feed travel ($l_f = 71$ mm) are depicted.

The comparison of the SEM-images shows signs of ploughing during the tool's entry into material for all materials. These are most distinct for the reference material, HS L-DED tends to show the least amount of ploughing.

In Fig. 12, the mean values and standard deviation of the burr area at the beginning ($l_f = 4$ mm) and at the end ($l_f = 68$ mm) of the feed travel are shown. For this purpose, the values of both measurements within a single slot (at the beginning and at the end) were averaged. Repetition 3 of micro milling reference material was not considered in Fig. 12 due to tool breakage. At the beginning of the feed travel ($l_f = 4$ mm), values of burr area in the same order of magnitude were determined for all materials. The burr area of HS L-DED (3341 ± 337 µm^2) and reference material (3578 ± 970 µm^2) reach similar levels, whereas L-PBF material (1964 ± 398 µm^2) tends to exhibit lower values of burr area.

After completing the feed travel, a distinct change in the amount of burr formation was noticed in dependence on the machined material. Machining L-PBF and HS L-DED materials shows no significant change in burr area after reaching the feed travel, whereas an increase in burr area was observed during micro milling of reference material. It is assumed that the stronger increase in burr formation when machining reference material is due to a more promoted plastic deformation, as also seen by ploughing in Fig. 11. This promoted plastic deformation can be attributed to the different tool wear and material properties of AM and reference materials. Burr is equivalent to non-seperated chips at the beginning (up milling side) and end (down milling side) of the tool's engagement during its rotation. The higher tool wear of micro end mills used for machining of reference material leads to a more rounded cutting edge. Higher cutting edge radii increase the minimum chip thickness required to prevent ploughing. Thus, tool wear increases plastic deformation during machining and hence is a reason for promoted burr formation. In addition, reference materials are significantly more ductile, which favors ploughing during machining even more.

7 Conclusion and outlook

In this study, the hybrid manufacturing of different additively manufactured AISI 316L is investigated and compared to the machining of equally specified reference material produced by continuous casting. For additive manufacturing (AM), high-speed laser directed energy deposition (HS L-DED) and laser-based powder bed fusion (L-PBF) were used. All materials were characterized in terms of relative density, microhardness, melt path dimensions as well as grain size and orientation. The different produced materials were subsequently machined by micro milling with tool diameters of $d = 100$ µm. The results of machining were evaluated based on tool wear, specific resultant forces, surface quality and burr formation. During our investigations, the following observations were made:

- The type of tool wear differs depending on the manufacturing method of the materials. Reference material tends to form build-up edges and noticeable cutting edge rounding (abrasive wear), whereas additively produced materials predominantly lead to adhesions on the tool.
- With regard to specific resultant forces, overlapping effects of grain and melt path structure during machining of additively manufactured materials were identified. Reference material exhibited increased cutting forces due to increased ploughing.
- The amount of burr formation and the surface quality depend on the material properties. Ductile reference material leads to smearing at the surface. AM materials, regardless of the production method used, are more brittle and show nearly ideal kinematic roughness on the produced surface.

Based on these results, the following conclusions about hybrid manufacturing of AM materials were drawn:

- Additively manufactured workpieces generally have different material properties compared to reference materials. Since tool wear, surface quality and burr formation depend on these material properties, machining of AM materials is consequently different compared to reference materials.
- Due to modified melt path and grain structures, specific resultant forces differ with regard to the AM process used for the generation of the material.

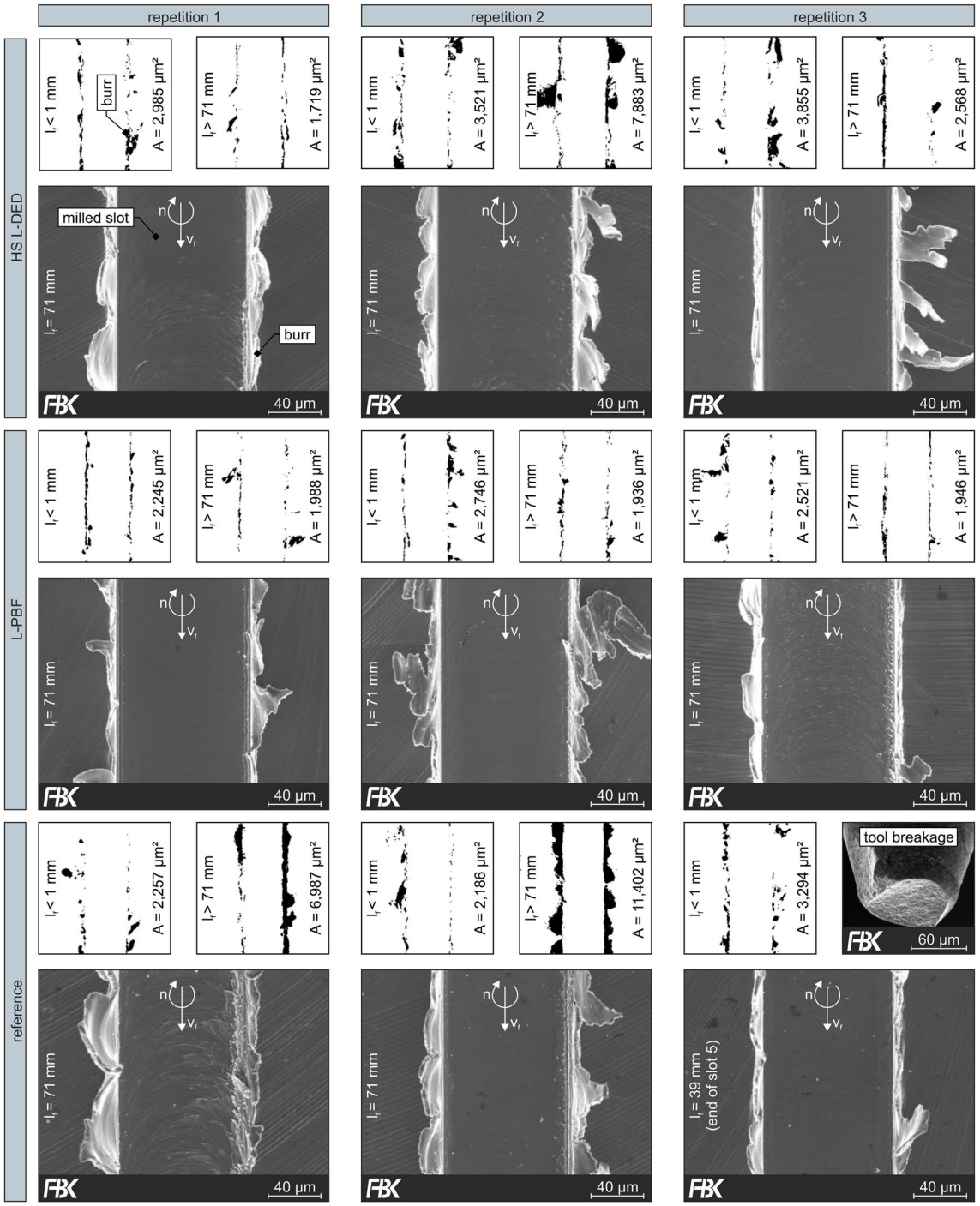

Fig. 11 Binary burr classification ($l_f < 1$ mm and $l_f > 71$ mm) and SEM-images ($l_f = 71$ mm)

In future studies, the underlying mechanisms in the machining of AM materials will be investigated in order to further understand the effects of grain and melt path structure during cutting. For this purpose, light microscope and EBSD images will be used to determine the exact grain orientation of the machined grains after micro milling. In addition, tool wear will be compared on the basis of quantitative data of cutting edge radii by means of atomic force microscope measurements.

*Naming of specific manufacturers is done solely for the sake of completeness and does not necessarily imply an endorsement of the named companies nor that the products are necessarily the best for the purpose.

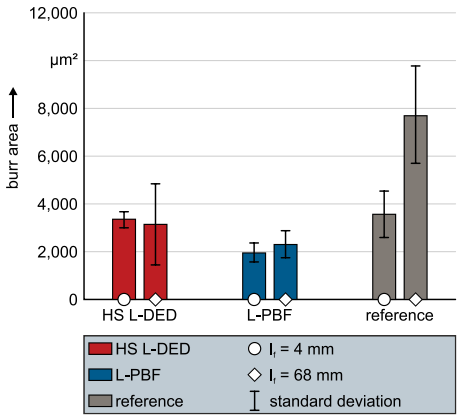

Fig. 12 Mean value of burr area at the beginning and end of the feed travel

Funding Open Access funding enabled and organized by Projekt DEAL. The authors would like to thank the EU European Regional Development Fund (ERDF) and the Ministry of Economics, Transport, Agriculture and Viticulture of the State of Rhineland-Palatinate for the financial support within the project "Center for Applied Additive Manufacturing with High-Speed Laser Directed Energy Deposition". Further thanks are addressed to the Fraunhofer Institute for Laser Technology (ILT) for providing HS L-DED samples.

References

1. Gebhardt A (2016) Additive Fertigungsverfahren: Additive Manufacturing und 3D-Drucken für prototyping—tooling—produktion, 5, neu bearbeitete und, erweiterte. Hanser, Ciando, München
2. Schmidt M, Merklein M, Bourell D, Dimitrov D, Hausotte T, Wegener K, Overmeyer L, Vollertsen F, Levy GN (2017) Laser based additive manufacturing in industry and academia. CIRP Ann 66:561–583. https://doi.org/10.1016/j.cirp.2017.05.011
3. Künneke T, Zimmer D (2017) Funktionsintegration additiv gefertigter Dämpfungsstrukturen bei Biegeschwingungen. In: Richard HA, Schramm B, Zipsner T (eds) Additive Fertigung von Bauteilen und Strukturen. Springer Fachmedien Wiesbaden, Wiesbaden, pp 61–74. https://doi.org/10.1007/978-3-658-17780-5_4
4. Delgado J, Ciurana J, Rodríguez CA (2012) Influence of process parameters on part quality and mechanical properties for DMLS and SLM with iron-based materials. Int J Adv Manuf Technol 60:601–610. https://doi.org/10.1007/s00170-011-3643-5
5. Greco S, Gutzeit K, Hotz H, Kirsch B, Aurich JC (2020) Selective laser melting (SLM) of AISI 316L—impact of laser power, layer thickness, and hatch spacing on roughness, density, and microhardness at constant input energy density. Int J Adv Manuf Technol 108:1551–1562. https://doi.org/10.1007/s00170-020-05510-8
6. Kaynak Y, Kitay O (2018) Porosity, surface quality, microhardness and microstructure of selective laser melted 316L stainless steel resulting from finish machining. JMMP 2:36. https://doi.org/10.3390/jmmp2020036
7. Dilberoglu UM, Gharehpapagh B, Yaman U, Dolen M (2021) Current trends and research opportunities in hybrid additive manufacturing. Int J Adv Manuf Technol 113:623–648. https://doi.org/10.1007/s00170-021-06688-1
8. Silva M, Felismina R, Mateus A, Parreira P, Malça C (2017) Application of a hybrid additive manufacturing methodology to produce a metal/polymer customized dental implant. Proc Manuf 12:150–155. https://doi.org/10.1016/j.promfg.2017.08.019
9. Kamath C, El-dasher B, Gallegos GF, King WE, Sisto A (2014) Density of additively-manufactured, 316L SS parts using laser powder-bed fusion at powers up to 400 W. Int J Adv Manuf Technol 74:65–78. https://doi.org/10.1007/s00170-014-5954-9
10. Choo H, Sham K-L, Bohling J, Ngo A, Xiao X, Ren Y, Depond PJ, Matthews MJ, Garlea E (2019) Effect of laser power on defect, texture, and microstructure of a laser powder bed fusion processed 316L stainless steel. Mater Des 164:107534. https://doi.org/10.1016/j.matdes.2018.12.006
11. Aboulkhair NT, Everitt NM, Ashcroft I, Tuck C (2014) Reducing porosity in AlSi10Mg parts processed by selective laser melting. Addit Manuf 1–4:77–86. https://doi.org/10.1016/j.addma.2014.08.001
12. Acevedo R, Sedlak P, Kolman R, Fredel M (2020) Residual stress analysis of additive manufacturing of metallic parts using ultrasonic waves: state of the art review. J Mater Res Technol 9:9457–9477. https://doi.org/10.1016/j.jmrt.2020.05.092
13. DebRoy T, Wei HL, Zuback JS, Mukherjee T, Elmer JW, Milewski JO, Beese AM, Wilson-Heid A, De A, Zhang W (2018) Additive manufacturing of metallic components—process, structure and properties. Prog Mater Sci 92:112–224. https://doi.org/10.1016/j.pmatsci.2017.10.001
14. Gibson I (2021) Additive manufacturing technologies, 3rd edn. Springer International Publishing AG, Cham
15. de Oliveira Campos F, Araujo AC, Jardini Munhoz AL, Kapoor SG (2020) The influence of additive manufacturing on the micromilling machinability of Ti6Al4V: a comparison of SLM and commercial workpieces. J Manuf Process 60:299–307. https://doi.org/10.1016/j.jmapro.2020.10.006
16. Kallel A, Duchosal A, Hamdi H, Altmeyer G, Morandeau A, Méo S (2020) Analysis of the surface integrity induced by face milling of laser metal deposited Ti-6Al-4V. Proc CIRP 87:345–350. https://doi.org/10.1016/j.procir.2020.02.030
17. Cheng K, Huo D (eds) (2013) Micro-cutting: fundamentals and applications. Wiley, Chichester. https://doi.org/10.1002/9781118536605
18. Mian A, Driver N, Mativenga PT (2011) Identification of factors that dominate size effect in micro-machining. Int J Mach Tools Manuf 51:383–394. https://doi.org/10.1016/j.ijmachtools.2011.01.004
19. Albrecht P (1960) New developments in the theory of the metal-cutting process: part I. the ploughing process in metal cutting. J Eng Ind 82:348–357. https://doi.org/10.1115/1.3664242
20. Aramcharoen A, Mativenga PT (2009) Size effect and tool geometry in micromilling of tool steel. Precis Eng 33:402–407. https://doi.org/10.1016/j.precisioneng.2008.11.002

21. Kieren-Ehses S, Böhme L, Morales-Rivas L, Lösch J, Kirsch B, Kerscher E, Kopnarski M, Aurich JC (2021) The influence of the crystallographic orientation when micro machining commercially pure titanium: a size effect. Precis Eng 72:158–171. https://doi.org/10.1016/j.precisioneng.2021.04.007
22. Ali H, Ghadbeigi H, Mumtaz K (2018) Effect of scanning strategies on residual stress and mechanical properties of selective laser melted Ti6Al4V. Mater Sci Eng A 712:175–187. https://doi.org/10.1016/j.msea.2017.11.103
23. Li T, Zhang L, Bultel GGP, Schopphoven T, Gasser A, Schleifenbaum JH, Poprawe R (2019) Extreme high-speed laser material deposition (EHLA) of AISI 4340 steel. Coatings 9:778. https://doi.org/10.3390/coatings9120778
24. Schopphoven T, Gasser A, Backes G (2017) EHLA: extreme high-speed laser material deposition. LTJ 14:26–29. https://doi.org/10.1002/latj.201700020
25. Schaible J, Sayk L, Schopphoven T, Schleifenbaum JH, Häfner C (2021) Development of a high-speed laser material deposition process for additive manufacturing. J Laser Appl 33:12021. https://doi.org/10.2351/7.0000320
26. Čapek J, Machová M, Fousová M, Kubásek J, Vojtěch D, Fojt J, Jablonská E, Lipov J, Ruml T (2016) Highly porous, low elastic modulus 316L stainless steel scaffold prepared by selective laser melting. Mater Sci Eng C Mater Biol Appl 69:631–639. https://doi.org/10.1016/j.msec.2016.07.027
27. DIN (2018) DIN EN ISO 6507-1:2018-07, Metallische Werkstoffe—Härteprüfung nach Vickers—Teil 1: Prüfverfahren. Beuth Verlag GmbH, Berlin. https://doi.org/10.31030/2778746
28. Ma M, Wang Z, Zeng X (2017) A comparison on metallurgical behaviors of 316L stainless steel by selective laser melting and laser cladding deposition. Mater Sci Eng A 685:265–273. https://doi.org/10.1016/j.msea.2016.12.112
29. Vilaro T, Colin C, Bartout JD, Nazé L, Sennour M (2012) Microstructural and mechanical approaches of the selective laser melting process applied to a nickel-base superalloy. Mater Sci Eng A 534:446–451. https://doi.org/10.1016/j.msea.2011.11.092
30. Attanasio A, Gelfi M, Pola A, Ceretti E, Giardini C (2013) Influence of material microstructures in micromilling of Ti6Al4V alloy. Materials (Basel) 6:4268–4283. https://doi.org/10.3390/ma6094268
31. Popov KB, Dimov SS, Pham DT, Minev RM, Rosochowski A, Olejnik L (2006) Micromilling: material microstructure effects. Proc Inst Mech Eng Part B J Eng Manuf 220:1807–1813. https://doi.org/10.1243/09544054JEM683
32. Kieren-Ehses S, Mayer T, Kirsch B, Aurich JC (2021) Atomic force microscope for in situ micro end mill characterization—part I: integration into a desktop sized machine tool. In: Euspen's 21th international conference & exhibition, Copenhagen
33. Greco S, Kieren-Ehses S, Kirsch B, Aurich JC (2021) Micro milling of additively manufactured AISI 316L: impact of the layerwise microstructure on the process results. Int J Adv Manuf Technol 112:361–373. https://doi.org/10.1007/s00170-020-06387-3
34. DIN (2020) DIN EN ISO 25178-2:2020-02, Geometrische Produktspezifikation (GPS)—Oberflächenbeschaffenheit: Flächenhaft—Teil_2: Begriffe, Definitionen und Oberflächen-Kenngrößen (ISO/DIS_25178-2:2019); Deutsche und Englische Fassung prEN_ISO_25178-2:2019. Beuth Verlag GmbH, Berlin. https://doi.org/10.31030/3121675
35. Medeossi F, Sorgato M, Bruschi S, Savio E (2018) Novel method for burrs quantitative evaluation in micro-milling. Precis Eng 54:379–387. https://doi.org/10.1016/j.precisioneng.2018.07.007
36. Oettel H, Schumann H, Benkißer G, Bernthaler T, Cyrener K (2016) Metallografie: Mit einer Einführung in die Keramografie, 15. überarbeitete und erweiterte Auflage, 1. Nachdruck, korrigiert 2016. Wiley-VCH Verlag GmbH & Co. KGaA, Weinheim
37. Hall EO (1951) The deformation and ageing of mild steel: III discussion of results. Proc Phys Soc B 64:747–753. https://doi.org/10.1088/0370-1301/64/9/303
38. Alexeev VP, Balyakin AV, Khaimovich AI (2017) Influence of the direction of selective laser sintering on machinability of parts from 316L steel. IOP Conf Ser Mater Sci Eng 177:12120. https://doi.org/10.1088/1757-899X/177/1/012120
39. Facchini L, Magalini E, Robotti P, Molinari A, Höges S, Wissenbach K (2010) Ductility of a Ti-6Al-4V alloy produced by selective laser melting of prealloyed powders. Rapid Prototyp J 16:450–459. https://doi.org/10.1108/13552541011083371
40. Kempen K, Thijs L, van Humbeeck J, Kruth J-P (2012) Mechanical properties of AlSi10Mg produced by selective laser melting. Phys Proc 39:439–446. https://doi.org/10.1016/j.phpro.2012.10.059
41. Wang X, Wan J, Wang J, Zhu L, Ruan H (2019) Anomalous sudden drop of temperature-dependent Young's modulus of a plastically deformed duplex stainless steel. Mater Des 181:108071. https://doi.org/10.1016/j.matdes.2019.108071